Electron-nuclear dynamics of the one-electron nonlinear polyatomic molecule H_3^{2+} in ultrashort intense laser pulses

C. Lefebvre,* H. Z. Lu, S. Chelkowski, and A. D. Bandrauk†
Laboratoire de Chimie Théorique, Département de Chimie, Université de Sherbrooke, Sherbrooke, Québec, J1K 2R1 Canada
(Received 27 November 2013; published 6 February 2014)

A quantum description of the one-electron triangular H_3^{2+} molecular ion, beyond the Born-Oppenheimer approximation, is used to study the full influence of the nuclear motion on the high-intensity photoionization and harmonic generation processes. A detailed analysis of electron and proton motions and their time-dependent acceleration allows for identification of the main electron recollision events as a function of time-dependent configuration of the protons. High-order-harmonic generation photons are shown to be produced by single-electron recollision in the second half of the pulse envelope, which also induces a redshift in the harmonics, due to the rapid few-femtosecond motions of protons. Perpendicular harmonics are produced, in general, with a linearly polarized laser pulse parallel to a bond of the triangular molecule, and, in particular, the harmonics in the cutoff region are elliptically polarized. When the laser-pulse polarization is parallel to a symmetry axis of the triangular molecular ion, creation and destruction of the chemical bond perpendicular to the polarization is predicted on a near-femtosecond time scale.

DOI: 10.1103/PhysRevA.89.023403 PACS number(s): 33.80.Wz, 42.50.Ct, 42.50.Hz, 42.65.Ky

I. INTRODUCTION

Ultrafast quantum dynamic imaging of molecules is currently developing as a new science with the help of the most recent advances in laser technology [1]. To perform dynamic imaging of molecules, one has to take into account the different time scales in the motion of the particles within a molecule. Nuclei evolve on the time scale of the femtosecond (1fs = 10^{-15} s). For instance, by applying a femtosecond laser pulse of a few optical cycles, in the near-infrared spectral region, the ultrafast vibrational wave-packet dynamics in the dissociative ionization of the H_2 molecule has been probed successfully [2]. On the other hand, electrons evolve on the time scale of the attosecond (1 as = 10^{-18} s). Only recently have ultrashort laser pulses with such comparable durations been produced from the nonlinear and nonperturbative interaction of matter with light through the process of high-order-harmonic generation (HHG) in atoms [3] and molecules (MHOHG) [4]. In this process, an atom or a molecule is ionized by an intense femtosecond infrared laser pulse. The photoelectron is subsequently accelerated by the laser field. As the electric field changes phase within an optical cycle, the ionized electron changes its direction and recollides with the parent ion [3]. Alternatively, the electron may recollide with the neighboring ions at higher energies than recollision with the parent ion [4]. High-energy photons of the order N are emitted in the form of high-order harmonics of the carrier-wave frequency ω, with a maximum energy $N\hbar\omega = I_p + 3.17U_p$, where I_p is the ionization potential and U_p is the ponderomotive energy in atoms [3] and beyond for molecules [4]. The high order of generated harmonics is the current source of ultrashort pulses of duration of few as's, which can be used to image the electron dynamics in atoms and molecules [1,5].

Numerical simulations are playing an important role in the understanding of laser-matter interaction, in particular in quantum molecular dynamic imaging [1]. The exact description of molecular dynamics should include the correlated electron-nuclear motion. So far, large-scale numerical solutions of the multidimensional time-dependent Schrödinger equation (TDSE) have been used to simulate the nonlinear nonperturbative interaction of a one-electron linear polyatomic molecule with ultrashort laser pulses on time scales of both nuclear and electron motion. In particular, the linear H_3^{2+} one-electron ion has been studied in a one-dimensional (1D), static nuclei simulation [6], to establish in polyatomics the existence of a nonlinear phenomenon unique to molecules, i.e., charge resonance enhanced ionization (CREI) [7]. Using an exterior complex scaling transformed B-spline basis-set expansion, Bian *et al.* confirmed this phenomenon in the three-dimensional (3D) linear H_3^{2+} in [8]. The same problem was addressed numerically for the linear two-electron 1D H_3^+ system where enhanced ionization was shown to involve charge-transfer (CT) states [9]. The effect of nuclear motion was shown to substantially reduce electron-rescattering effects from H_3^{2+} to H_3^+ in the energy range up to $10U_p$ [10].

In the present work, we examine electron ionization and rescattering of the 2D nonlinear (triangular) one-electron H_3^{2+}. Coulomb explosion imaging of H_3^{2+} has been studied previously to monitor two- and three-body kinematical correlations in dissociative recombination of H_3^+ [11] due to the importance of this phenomena in low-energy plasmas [12] and in the chemistry of interstellar medium [13]. Laser-induced electron localization in H_3^{2+} in the equilateral configuration has recently been reported with Born-Oppenheimer simulations [14]. The H_3^+ ion has been recently shown to be formed by unusual proton-transfer mechanisms in organic molecules exposed to femtosecond intense laser pulses [15,16]. H_3^+ and H_3^{2+}, due to their unique equilateral triangular geometry, thus provide a fundamentally original system for the theoretical development of the nonperturbative response of nonlinear molecules to intense laser pulses, as recently pointed out in

*Present address: INRS-EMT, 1650 Boulevard Lionel-Boulet, Varennes, Québec, J3X 1S2, Canada; catherine.lefebvre@emt.inrs.ca
†andre.bandrauk@usherbrooke.ca

Coulomb explosion studies of $D_3{}^+$ [17–21]. The photophysics of simple trimers also allows for the study of full many-body dynamics such as Rydberg trimers [22] and quantum interferences in three-slit experiments [23]. Previous static nuclei 2D simulations of the two-electron $H_3{}^+$ [24] showed pronounced three-center interferences in the MHOHG spectrum, based on a three-center recollision model. Three-center electron interference effects have been shown to be operative in X_3 Jahn-Teller systems [25], as well as in recent quantum three-slit experiments [23].

In the present work, we examine, in detail, correlated electron-nuclear dynamics in the one-electron H_3^{2+} ion by a fully coupled electron-nuclear numerical simulation of the corresponding TDSE in 2D, allowing us to monitor electron-proton dynamics from the attosecond to femtosecond time scale. We study the effect of the alignment of the linearly polarized few-cycle pulse on the MHOHG. Not only do we observe that the high-order harmonics are redshifted and are produced mainly by one single recollision event in the second half of the pulse envelope, due to the rapid motion of the nuclei, but the harmonics are elliptically polarized (in the cutoff region) when the laser pulse is parallel to a bond of the triangular molecule. When the laser-pulse polarization is parallel to a symmetry axis of the triangular molecule, the electron cloud oscillation is indicative of creation and destruction of a chemical bond at every optical cycle.

II. NUMERICAL METHOD

We consider the one-electron molecular system H_3^{2+} in a nonlinear (triangular) configuration in a 2D plane. The nuclear coordinates are defined with Jacobi coordinates r, which is the relative coordinate between two nuclei forming the basis of the triangle, and R, which is the relative coordinate between the upper nucleus and the center of mass of the two base nuclei, as shown in Fig. 1(a). The angle between these two Jacobi coordinates is fixed to $\theta = 90^\circ$ as occurs in C_{2v} symmetry, i.e., an isosceles triangle, as we anticipate that this is the main direction of Coulomb explosion. The nuclear coordinates are related to Cartesian coordinates as follows: $x_{N_1} = 0, y_{N_1} = \frac{2}{3}R, x_{N_2} = -\frac{1}{2}r, y_{N_2} = -\frac{1}{3}R, x_{N_3} = \frac{1}{2}r, y_{N_3} = -\frac{1}{3}R$. The electron coordinates are defined with polar coordinates ϕ and ρ, corresponding to Cartesian coordinates $\rho = \sqrt{x_e^2 + y_e^2}$ and $\phi = \arccos(x_e/\rho)$ [24]. Details of the coordinate transformation and of the Hamiltonian are presented in Appendices A and B.

The complete equation of motion of the 2D molecular ion H_3^{2+} is described by the time-dependent Schrödinger equation (TDSE) (in atomic units, $e = \hbar = m_e = 1$) beyond the Born-Oppenheimer approximation,

$$i\hbar\frac{\partial}{\partial t}\Psi(\rho,\phi,r,R,t) = [T_e + T_N + V(\rho,\phi,r,R,t)]\Psi(\rho,\phi,r,R,t), \quad (1)$$

with the kinetic-energy operators

$$T_e = -\frac{1}{2\mu_e}\left[\frac{1}{\rho}\frac{\partial}{\partial\rho}\rho\frac{\partial}{\partial\rho} + \frac{1}{\rho^2}\frac{\partial^2}{\partial\phi^2}\right],$$
$$T_N = -\frac{1}{2\mu_r}\frac{\partial^2}{\partial r^2} - \frac{1}{2\mu_R}\frac{\partial^2}{\partial R^2}, \quad (2)$$

and the total potential

$$V(\rho,\phi,r,R,t) = V_{eN}(\rho,\phi,r,R) + V_{NN}(r,R) + V_{\rm int}(\rho,\phi,t). \quad (3)$$

The electron-nuclei attraction V_{eN}, the nuclear repulsion V_{NN}, and the laser interaction $V_{\rm int}$ potentials are, respectively, given by

$$V_{eN}(\rho,\phi,r,R) = -\sum_{k=1}^{3}\frac{1}{\sqrt{\rho^2 + x_{N_k}(r)^2 + y_{N_k}(R)^2 - 2\rho[\cos\phi x_{N_k}(r) + \sin\phi y_{N_k}(R)] + c_{en}}}, \quad (4a)$$

$$V_{NN}(r,R) = \sum_{k,l=1,\ldots,3}^{k<l}\frac{1}{\sqrt{[x_{N_k}(r) - x_{N_l}(r)]^2 + [y_{N_k}(R) - y_{N_l}(R)]^2 + c_{NN}}}, \quad (4b)$$

$$V_{\rm int}(\phi,\rho,t) = -DE(t), \quad E(t) = \epsilon(t)\cos(\omega t + \varphi). \quad (4c)$$

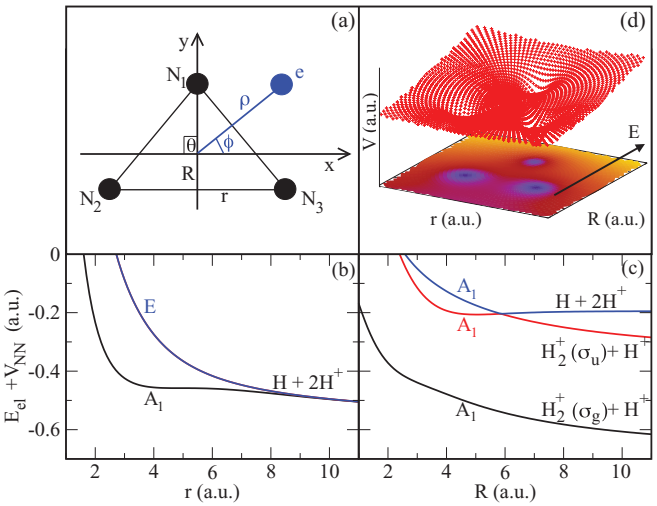

FIG. 1. (Color online) (a) Geometry of the H_3^{2+} molecular ion in the xy plane with the origin at the center of mass of the nuclei. The nuclear coordinates are r, R, and θ (in black) and the electron coordinates are ρ and ϕ (in blue). Potential-energy curve of the ground electronic state and the first two excited electronic states of H_3^{2+} as a function of the nuclear distance in (b) a D_{3h} configuration (equilateral triangle) with $R = \sin(\pi/3)r$ and (c) a C_{2v} configuration (isosceles triangle) as a function of R with fixed $r = 2.5$ a.u. (d) Potential in a D_{3h} symmetry at $r = 5$ a.u. at field strength $\vec{E}||Oy$, $E = 9.2 \times 10^{-2}$ a.u. (intensity $I = 3 \times 10^{14}$ W/cm^2, y polarization) corresponding to $m = 1$ in Fig. 4.

The reduced masses in the kinetic operators T_e and T_N, in Eq. (2), are defined as

$$\mu_e = \frac{m_{N_1} + m_{N_2} + m_{N_3}}{1 + m_{N_1} + m_{N_2} + m_{N_3}}, \quad \mu_r = \frac{m_{N_2} m_{N_3}}{m_{N_2} + m_{N_3}},$$
$$\mu_R = \frac{m_{N_1}(m_{N_2} + m_{N_3})}{m_{N_1} + m_{N_2} + m_{N_3}}, \tag{5}$$

with $m_{N_i}, i = 1, \ldots, 3$, denoting the mass of the three nuclei. The three potentials in Eqs. (4a) and (4b) thus couple completely electron-proton motion. In the attraction and repulsion potentials in Eqs. (4a) and (4b), we use Coulomb softening parameters $c_{eN} = 0.35$ and $c_{NN} = 1$, which gives potentials for H_3^+ in good agreement with experimental geometries [24]. D is the dipole, here expressed as $D = -\rho\cos(\phi)$ and rigorously defined in Appendix A [Eq. (A8)]. The electric laser pulse for the radiative interaction $V_{\rm int}$, given by Eq. (4c), is linearly polarized. In the case of a polarization along the x axis (labeled $\vec{E}||Ox$), $V_{\rm int} = xE(t)$, while for polarization along the y axis (labeled $\vec{E}||Oy$), $V_{\rm int} = yE(t)$, with an electric-field strength $E(t)$. ω is the carrier-wave frequency [$\omega = 2\pi c/(\lambda = 800\ \text{nm}) = 0.057$ a.u.] of period $T = 2\pi/\omega$=2.7 fs, $\varphi = 0$ is the carrier-envelope phase (CEP), and $\epsilon(t)$ is the laser-pulse envelope of trapezoidal shape with two optical cycles that are ramp on, two constant optical cycles at intensity $I = E_0^2 = 3 \times 10^{14}$ W/cm^2(9.2×10^{-2} a.u.), and two optical cycles that are ramp off, as depicted in Fig. 2(a). Recent experiments

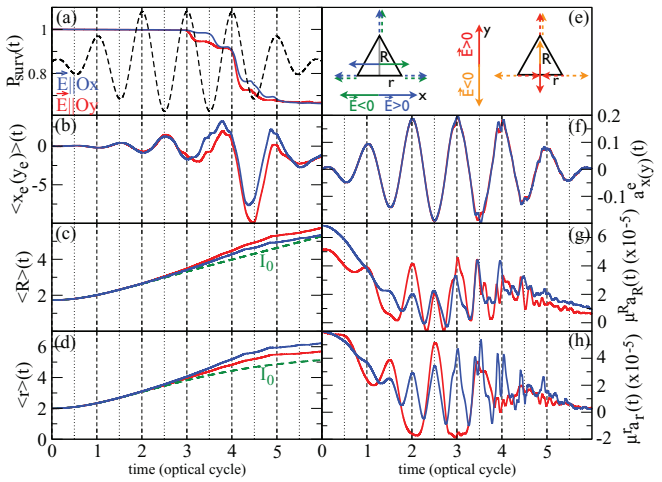

FIG. 2. (Color online) Left panels: (a) Survival probability ($\vec{E}||Ox$ in blue, $\vec{E}||Oy$ in red) and electric laser pulse (black dashed line) as a function of time. (b) Electron dipole along the x (for $\vec{E}||Ox$, blue line) and y (for $\vec{E}||Oy$, red line) direction. (c),(d) Nuclear displacements along the R and r coordinates, respectively ($\vec{E}||Ox$ in blue, $\vec{E}||Oy$ in red). Dashed green line is for the zero-field ($I = 0$) case. Right panels: (e) Electron (solid lines) and nuclei (dashed lines) displacement induced by a $\vec{E}||Ox$ ($E > 0$ in blue, $E < 0$ in green) and $\vec{E}||Oy$ ($E > 0$ in red, $E < 0$ in orange) pulse. (In the case of $\vec{E}||Oy > 0$, the electron can be localized on the two lower protons, strengthening the chemical bond along the r coordinate.) (f)–(h) Acceleration $a(t)$ of the electron in the x (for $\vec{E}||Ox$, blue line) and y (for $\vec{E}||Oy$, red line) direction and of the nuclei along the R and r coordinates, respectively. Laser-pulse conditions: $I = 3 \times 10^{14}$ W/cm^2, $\omega = 0.057$ a.u., $\lambda = 800$ nm, $T = 2.7$ fs, six optical cycles.

have shown that the ionization probability for H_3^+ is most favorable with a linearly polarized laser pulse aligned along $\vec{E}||Ox$ and $\vec{E}||Oy$ [17,18]. Our choice of nuclear coordinates thus corresponds with the laser orientation along the r or R nuclear coordinate (x or y axis) (see Fig. 1), describing motion from D_{3h} to C_{2v} symmetry.

The initial molecular wave function is defined by $\Psi(\rho,\phi,r,R,t=0) = f(r,R)\Phi(\rho,\phi;r,R)$, where $\Phi(\rho,\phi;r,R)$ is the electronic eigenfunction at fixed nuclear coordinates r and R obtained by imaginary-time propagation [26,27]. $f(r,R)$ is the initial three-proton function in terms of the nuclear coordinates centered at $r = 2$ a.u., $R = 1.73$ a.u., and describes a Franck-Condon transition from H_3^+ to H_3^{2+} at the equilibrium distance $r_{eq}(H_3^+) = 2$ a.u. [28–30]. For each fixed nuclear coordinate, the electronic potential-energy surfaces (PESs) are calculated from the laser-free TDSE, given by Eq. (1), i.e., $V_{\rm int} = 0$. Illustrated in Figs. 1(b) and 1(c) are cuts of the Born-Oppenheimer (static nuclei) PESs for nuclear configurations in D_{3h} symmetry (equilateral triangle) [Fig. 1(b)] and in C_{2v} symmetry (isosceles triangle), with r fixed at 2.5 a.u. [Fig. 1(c)]. In D_{3h} symmetry, the two first excited states are degenerate and the ground state as well as the excited states are dissociative, with a single dissociation channel $H + 2H^+$. In C_{2v} symmetry, the degeneracy of the excited states is lifted, although these two states cross at specific internuclear distances $R = \sin(\pi/3)r$, thus creating a "conical" intersection seam in the PESs. The three distinct dissociative states give rise to three different dissociation channels: (1) $H_2^+(1\sigma_g) + H^+$, (2) $H_2^+(1\sigma_u) + H^+$, and (3) $H + 2H^+$. We note that between $R = r = 3.5$ and 4 a.u., there is a resonant three-photon transfer to the degenerate E state. McKenna *et al.* [17] have concluded that the D_3^{2+} ion ionizes preferentially at this configuration, in agreement with our calculations; see Fig. 2(a).

The TDSE is solved numerically using a second-order split-operator spectral method for the time discretization and a spectral method combined with the finite-difference method for the spatial discretization in order to reduce, as much as possible, the grid sizes [31]. The time step is set at $\delta t = 0.05$ a.u., with an electron grid of size $\rho < \rho_{\max} = 128$ a.u. with 512 points and angle $0 < \phi < 2\pi$ with 128 points. The proton grid is chosen of size $r < r_{\max}$ and $R < R_{\max} = 19.2$ a.u. with 192 points in both r and R directions. For very short pulses, as considered here, it has been verified that the nuclear wave function is contained within the grid at all times, and that the electron grid size $\rho_{\max}$ is always larger than the maximum ionized electron field-induced trajectory defined by $\alpha = E/\omega^2$ in a laser field of amplitude E and frequency ω. Thus, at $I = 3 \times 10^{14}$ W/cm^2(9.2×10^{-2} a.u.) and $\omega = 0.057$ a.u., $\alpha = 28$ a.u. $\ll \rho_{\max}$. Absorbing boundaries at the grid extrema are used ensuring that a measurable population reaches the absorbing boundaries during the propagation.

During the time propagation, the total survival probability at any time t is obtained from

$$P_{\rm surv}(t) = \int_0^{+\rho_{\max}} \rho d\rho \int_0^{2\pi} d\phi \int_0^{\infty} dr \times \int_0^{\infty} dR |\Psi(\rho,\phi,r,R,t)|^2, \tag{6}$$

the corresponding electron density,

$$P_e(\rho,\phi,t) = \int_0^\infty dr \int_0^\infty dR |\Psi(\rho,\phi,r,R,t)|^2, \quad (7)$$

the time-dependent electron dipole,

$$\langle x(y)_e\rangle(t) = \int_0^{+\rho_{\max}} \rho d\rho \int_0^{2\pi} d\phi \int_0^\infty dr \times \int_0^\infty dR |\Psi(\rho,\phi,r,R,t)|^2 (-x(y)_e), \quad (8)$$

and the time-dependent nuclear displacement,

$$\langle R(r)\rangle(t) = \int_0^{+\rho_{\max}} \rho d\rho \int_0^{2\pi} d\phi \times \int_0^\infty dr(R) |\Psi(\rho,\phi,r,R,t)|^2 R(r). \quad (9)$$

The laser-induced acceleration is used for calculating the MHOHG spectrum due to its accuracy, avoiding large dipoles from ionized electrons [32],

$$a^e_{x(y)}(t) = \int \rho d\rho \int d\phi \int dR \int dr \Psi^*(\rho,\phi,r,R,t) \times \left[-\frac{\partial H}{\partial x(y)_e}\right] \Psi(\rho,\phi,r,R,t), \quad (10a)$$

$$-\frac{\partial H}{\partial x(y)_e} = -\frac{\partial V_{eN}}{\partial x(y)_e} - E(t). \quad (10b)$$

A Hanning filter is used to eliminate spurious background effects in the plateau region [33]. The Fourier transform of the time-dependent acceleration gives the MHOHG power spectrum for a six-cycle pulse of duration T,

$$P^e_{x(y)}(\omega) \propto \left| \int_0^{6T} a^e_{x(y)}(t) \exp(-i\omega t) dt \right|^2. \quad (11)$$

As for the experimental measure, the total MHOHG yield for a given laser polarization would be the sum of $P^e_x(\omega)$ and $P^e_y(\omega)$. Since a simple classical model predicts that harmonic generation occurs by electron recollision with the parent ion [3,5], a time-series analysis provides a time profile of the harmonics and recollision times [33,34],

$$d_G(\omega,t) = \int_{-\infty}^\infty \exp(-i\omega t') \exp\left[-\frac{(t-t')^2}{2\sigma_0^2}\right] a^e(t') dt', \quad (12)$$

where $\sigma_0 = 0.1$ fs is the width of the Gaussian time window in the Gabor transform. This corresponds to a frequency spread of $\Delta\omega$ of about ten harmonics.

Complementary to these observables, the nuclear acceleration, corresponding to the forces acting on the protons, can also be evaluated as

$$\mu_{R(r)} a^{R(r)}(t) = \int \rho d\rho \int d\phi \int dR \int dr \Psi^*(\rho,\phi,r,R,t) \times \left[-\frac{\partial H}{\partial R(r)}\right] \Psi(\rho,\phi,r,R,t), \quad (13a)$$

$$-\frac{\partial H}{\partial R(r)} = -\frac{\partial V_{eN}}{\partial R(r)} - \frac{\partial V_{NN}}{\partial R(r)}, \quad (13b)$$

on which the Fourier transform and the time-frequency analysis can also be performed, thus providing complementary mathematical results for a detailed time analysis of the corresponding physics of the proton dynamics coupled to the electron dynamics [35].

III. RESULTS AND DISCUSSION

A. Particle dynamics

The complex non-Born-Oppenheimer dynamics of the dissociating one-electron H_3^{2+} molecular ion in the presence of an ultrashort (few cycles) and intense laser pulse can be observed in the survival probability $P_{\text{surv}}(t)$ [Eq. (6)], as shown in Fig. 2(a). During the first optical cycle, the molecule is in a D_{3h} configuration in which the nuclei are at short internuclear distances, starting at $r = 2$ a.u., $R = 1.73$ a.u., where chemical bonding dominates. The nuclei move to larger distances due to laser-induced vibrational excitation and nuclear repulsion. The laser-field interaction then becomes stronger compared to the total Coulomb potential and the molecule starts to ionize. A survival probability less than one means that some portion of the total wave function on the electronic grid ($\rho \times \phi$) has been absorbed at the absorbing boundary ($\rho_{\max} = 128$). This corresponds to ionization of the direct electron that would not recollide with the parent ion. We observe the direct ionization probability [blue and red solid lines in Fig. 2(a)] to increase at each peak of the laser pulse after three optical cycles. Although the final $P_{\text{surv}}(t_f = 6T)$ is independent of the laser-field polarization, the ionization events occur differently during the laser pulse. The ionization is relatively more important at $t = 3T$ and $4T$ (when $E > 0$) for $\vec{E}||Oy$, perpendicular to one H–H (N_2–N_3) bond. At $t = 3.5T$ and $4.5T$ (when $E < 0$), it is more important for $\vec{E}||Ox$, parallel to that bond. In both cases, it is at $t = 4T$ that the most efficient ionization occurs.

These electron dynamics can also be observed in the electron dipole along the laser polarization (i.e., $\langle x_e\rangle$ for $\vec{E}||Ox$ and $\langle y_e\rangle$ for $\vec{E}||Oy$), given by Eq. (8) [Fig. 2(b)], and the electron acceleration (i.e., a^e_x for $\vec{E}||Ox$ and a^e_y for $\vec{E}||Oy$), given by Eq. (10a) [Fig. 2(f)]. The ionization of the molecular ion induces an additional dephasing in the dipole, which appears earlier for $\langle y_e\rangle$ than $\langle x_e\rangle$ due to the earlier ionization event with $\vec{E}||Oy$, and some deformation in the electron acceleration $a^e_{x(y)}$. We note that the dipole $\langle x(y)_e\rangle$ does not vanish at the end of the pulse due to the large dipole of ionized electrons [32], as opposed to the acceleration. The electron response is illustrated by a time-dependent electron density in Figs. 3 and 4, for the x and y polarization, respectively, where each panel corresponds to the electronic-density snapshot at times $t = (m+n)T$, with $n = 0,1,2,3,4,5$ and $m = 0,1/4,1/2,3/4,1$, i.e., at a quarter of the cycles. One observes that the electronic density moves in opposite direction to the electric field, as expected from the classical potential $V_{\text{int}} = -DE(t)$, given by Eq. (4c). For instance, at $t = 3T$ ($m = 1, n = 2$) (when $E > 0$) with $\vec{E}||Ox$, the electron is localized on one proton (N_2), corresponding to the configuration $H + 2H^+$, while with $\vec{E}||Oy$, the electron is localized on two protons (N_2 and N_3) corresponding to the configuration $H_2^+ + H^+$. At the end of the six optical cycles of the laser pulse ($m = 1, n = 5$), the electron is

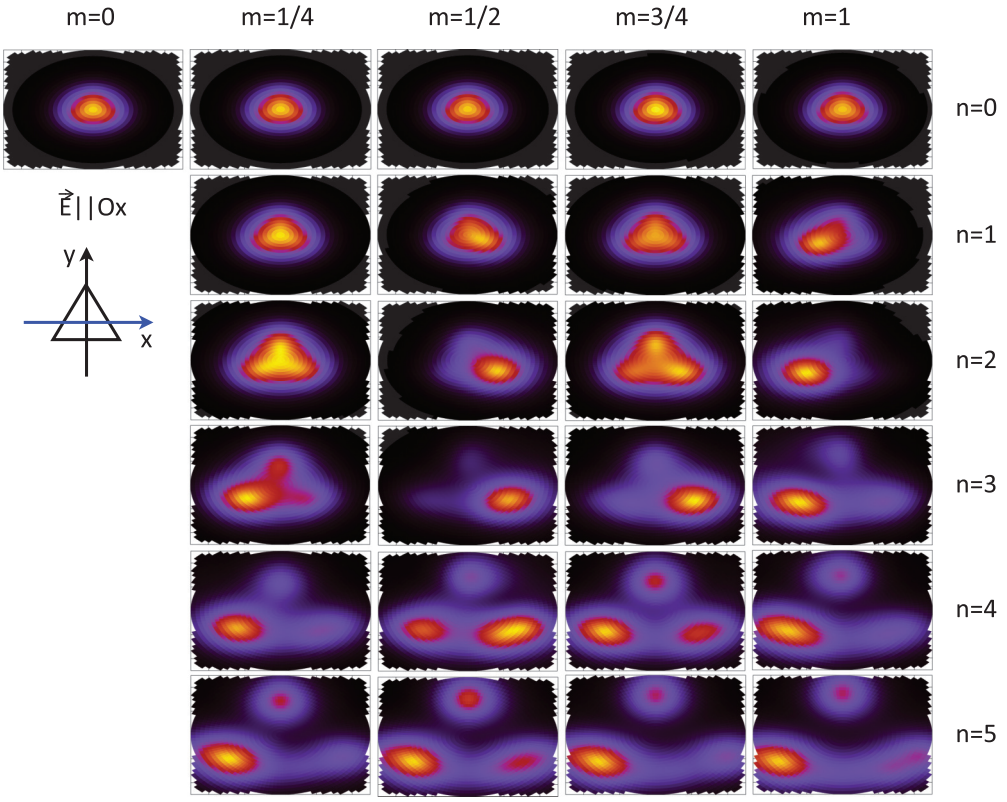

FIG. 3. (Color online) Snapshots of the electron density in the xy plane in an electric field $\vec{E}||Ox$ (x polarization) as a function of time $t = (m + n)T$, where $T = 2\pi/\omega$ ($E = 0$ at $m = 1/4,3/4$, $E < 0$ at $m = 1/2$, and $E > 0$ at $m = 1$).

localized preferentially on one proton in both polarizations and both direction $\pm E(t)$, i.e., forming $H + 2H^+$, the three-body breakup $3A_1$ channel [Fig. 1(c)].

The molecular ion is dissociative and the nuclei move rapidly via Coulomb explosion to larger internuclear distances preserving a near-D_{3h} symmetry, as can be seen in Figs. 2(c) and 2(d) [Eq. (9)] (green dashed lines for zero field). When the laser pulse is present, the nuclei are pushed even further (solid lines). For instance, with $\vec{E}||Oy$ at four optical cycles, when most of the ionization occurs, up to ≈25%, the nuclei have moved to $r = 4.8$ a.u. and $R = 4.2$ a.u. (from initial $r = 2$ a.u. and $R = 1.73$ a.u.). This implies velocities $\dot{r} = 0.7$ a.u./cycle (0.14 Å/fs), $\dot{R} = 0.6$ a.u./cycle (0.12 Å/fs). We observe that the protons move further along the r coordinate with $\vec{E}||Ox$ and along the R coordinate with $E||Oy$ (i.e., favored motion for the nuclear coordinate parallel to the laser-pulse polarization due to electron ionization along these directions). The corresponding proton accelerations, $\mu_R a^R(t)$ (N_1 motion) and $\mu_r a^r(t)$ (N_2–N_3 motion), given by Eq. (13a) [Figs. 2(g) and 2(h)], have mostly positive values due to important nuclear repulsion, and then tend to zero after four optical cycles. We note that $\mu_r a^r$ is minimal and negative for $\vec{E}||Oy > 0$. As seen in Fig. 4, this corresponds to $m = 1$, where the electron is being transferred by the field to the H–H (N_2–N_3) bond from N_1 [as sketched in Fig. 2(e), right]. This reinforces bonding, increasing the attraction between N_2–N_3. For $\vec{E}||Oy < 0$, corresponding to $m = 1/2$ in Fig. 4, the electron moves away from the H–H (N_2–N_3) bond, reducing bonding [as sketched in Fig. 2(e), right] and increasing repulsion between the two protons N_2–N_3 so that $\mu_r a^r > 0$. We also observe that the oscillation of $\mu_R a^R(t)$ (for $\vec{E}||Ox$ and $\vec{E}||Oy$) and $\mu_r a^r(t)$ (for $\vec{E}||Ox$ only) is of a frequency 2ω (periodicity of $2T$), i.e., with positive sign at each half cycle of the laser pulse, as compared to the electron acceleration oscillating at a periodicity of T. This is also observed in H_2^+ and explained by the displacement of the electron cloud between the protons, induced by the laser pulse of frequency ω at the field extrema ($E > 0$ and < 0) [35]. Such oscillation is also reported in Ref. [36] where an electric field of frequency ω induces tunnel ionization and the plasma density generated displays strong variations at every half cycle, causing a plasma current that oscillates at a frequency 2ω. Interestingly, when the laser pulse is $\vec{E}||Ox$ (parallel to the r coordinate), the electron cloud oscillates in the x axis and influences the three protons [as sketched in Fig. 2(e), left]. This is seen in the 2ω periodicity of both $\mu_r a^r(t)$ and $\mu_R a^R(t)$ (for $\vec{E}||Ox$). On the other hand, when the laser pulse is $\vec{E}||Oy$ (parallel to the R coordinate), the electron cloud oscillates between the upper proton (N_1) and N_2–N_3 [as sketched in Fig. 2(e), right]. Consequently, only $\mu_R a^R(t)$ oscillates with a periodicity of 2ω. $\mu_r a^r(t)$ oscillates with periodicity of ω, with opposite phase with the electron acceleration $a_y^e(t)$, and this is induced by the reinforcement of the N_2–N_3 bond every half cycle ($m = 1$), as mentioned above. Clearly, the nuclear motion is not only driven by the dissociative configuration of the ion, but is strongly correlated to the electron motion.

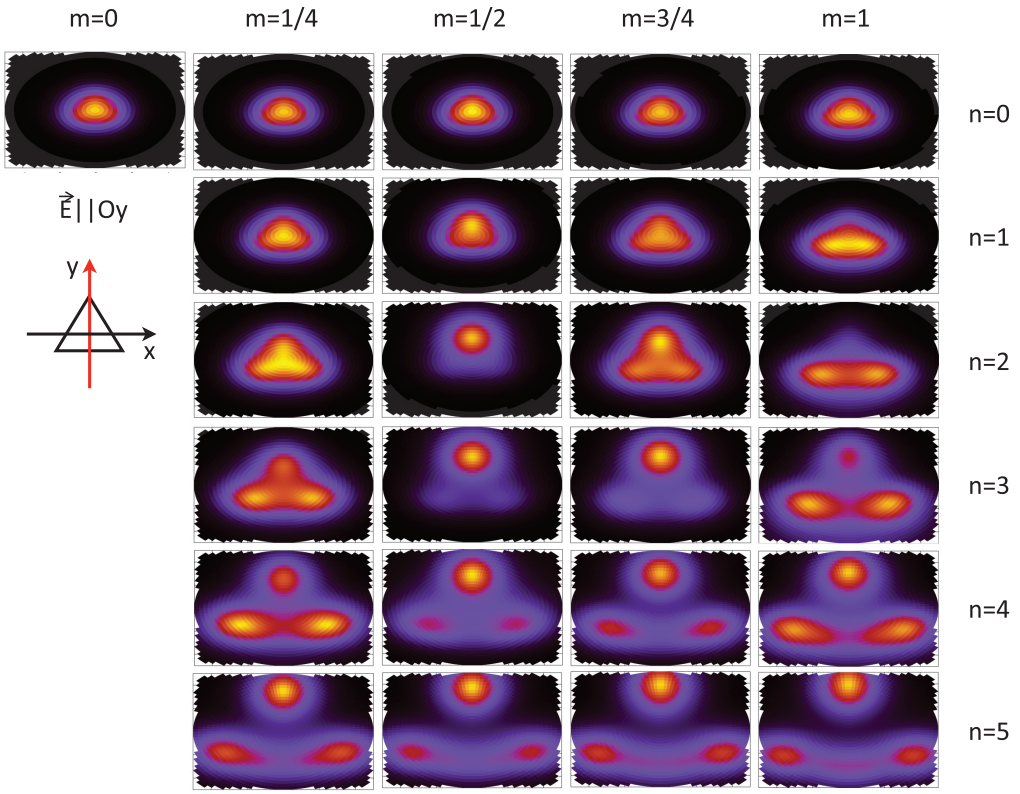

FIG. 4. (Color online) Snapshots of the electron density in the xy plane in an electric field $\vec{E}||Oy$ (y polarization) as a function of time $t = (m + n)T$, where $T = 2\pi/\omega$ ($E = 0$ at $m = 1/4,3/4$, $E < 0$ at $m = 1/2$, and $E > 0$ at $m = 1$).

B. Molecular high-order-harmonic generation

Following the classical recollision model [3,5], once the molecule is ionized, the photoelectron recombines with the ion, which leads to high-order harmonics. In Fig. 1(d), the potential of H_3^{2+} in a D_{3h} symmetry at $r = 5$ a.u., perturbed by a strong field along the R axis ($\vec{E}||Oy$, $E > 0$), shows the sites of recollision, indicative of possible interferences, which is not specifically studied here. The MHOHG spectrum, calculated from the electron acceleration $a^e_{x(y)}(t)$, given by Eq. (10a), is shown in Fig. 5 for $\vec{E}||Ox$ and in Fig. 6 for $\vec{E}||Oy$. The MHOHG spectra are calculated for the two components, $P^e_x(\omega)$ and $P^e_y(\omega)$, for each laser polarization. For comparison, Figs. 7 and 8 illustrate the MHOHG spectra for the static molecular ion at fixed geometry, $r = R = 5$ a.u., which is the geometry reached by the moving molecular ion at the main ionization event at around $t = 4T$ ($m = 1,n = 3$ of Figs. 3 and 4). First, similarities are observed in the MHOHG spectra for the dynamic and static cases with a plateau region followed by a cutoff, indicating that in the dynamic case, the harmonics are emitted when the nuclei have moved at large distances where the ionization yield is increasing. We recall that the ionization is enhanced at large distances: CREI occurs at $R \sim 6.5$ a.u. in conditions studied previously for a linear molecular ion [6], and a three-photon resonance exists at $R \sim 4$ a.u. in a D_{3h} configuration. The semiclassical electron recollision model [3,5] predicts the maximum harmonic order, $N_{\max}\omega = 3.17\,U_p + I_p = 55$, with the ponderomotive energy, $U_p = E_0^2/4\omega^2 = 0.658$ a.u., and the ionization potential $I_p = 1.029$ a.u., at $r = R = 5$ a.u. The predicted recollision energy value is close to the calculated $N_{\max} = 58$ in Figs. 5–8. The amplitude of the harmonic intensities is lower in the dynamic case due to the non-Born-Oppenheimer dynamics, where the fast proton motion reduces the electron recollision probability. We emphasize that the nuclei have moved, with $\vec{E}||Oy$ for instance, from initial $r = 2$ a.u., $R = 1.73$ a.u. to $r = 4.8$ a.u., $R = 4.2$ a.u., respectively, in four optical cycles,

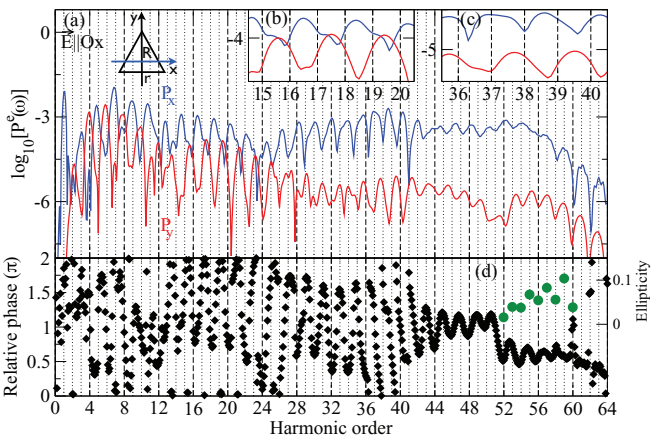

FIG. 5. (Color online) (a) Molecular high-order-harmonic (MHOHG) spectra of H_3^{2+} with moving nuclei [blue, $P^e_x(\omega)$ and red, $P^e_y(\omega)$], with (b),(c) zoom of the harmonics in the plateau region. (d) Relative phase of the harmonics (black diamonds) and ellipticity of the cutoff harmonics (green circles). Laser-pulse conditions: $\vec{E}||Ox$, $I = 3 \times 10^{14}$ W/cm^2, $\omega = 0.057$ a.u., $\lambda = 800$ nm, $T = 2.7$ fs, six optical cycles.

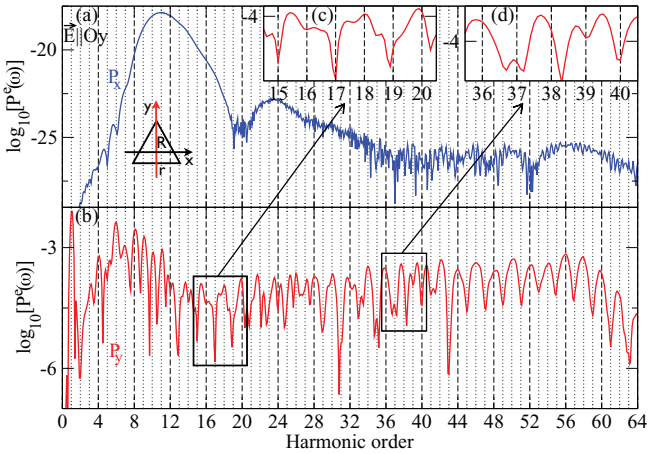

FIG. 6. (Color online) (a), (b) Molecular high-order-harmonic (MHOHG) spectra of H_3^{2+} with moving nuclei [blue, $P_x^e(\omega)$ and red, $P_y^e(\omega)$], with (c),(d) zoom of the harmonics in the plateau region for $P_y^e(\omega)$. Laser-pulse conditions: $\vec{E}||Oy$, $I = 3 \times 10^{14}$ W/cm^2, $\omega = 0.057$ a.u., $\lambda = 800$ nm, $T = 2.7$ fs, six optical cycles.

10.7 fs, whereas the electron recollision occurs every 2/3 cycle ≈ 1.8 fs [3,5]. Moreover, a splitting in the harmonics is observed in the static case (and also at various fixed geometries, not shown here), which is nearly absent in the dynamic case. The fractional-order harmonics have been reported in Ref. [37] and explained by contribution from excited states in the MHOHG process. This signature is smoothed out in the dynamic case because of the fast nuclear motion.

Second, we compare the two polarizations, $\vec{E}||Ox$ and $\vec{E}||Oy$. As expected, the harmonic cutoff position is independent of the laser-field polarization. Most strikingly, for $\vec{E}||Ox$, $P_x^e(\omega)$ and $P_y^e(\omega)$ show similar intensities, with an intensity of three orders higher (two orders higher for the static case) for the $P_x^e(\omega)$, parallel to the laser-pulse polarization. With such similar intensities of $P_x^e(\omega)$ and $P_y^e(\omega)$, we calculated the relative phase, for the dynamic case, between

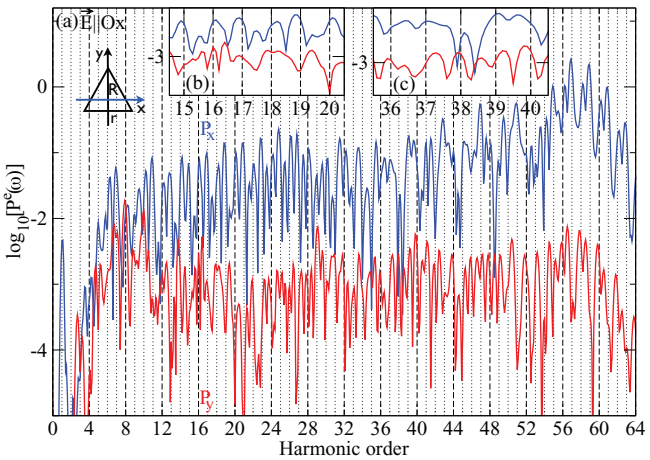

FIG. 7. (Color online) (a) Molecular high-order-harmonic (MHOHG) spectra of H_3^{2+} with fixed nuclei at $r = R = 5$ a.u. [blue, $P_x^e(\omega)$ and red, $P_y^e(\omega)$], with (b),(c) zoom of the harmonics in the plateau region. Laser-pulse conditions: $\vec{E}||Ox$, $I = 3 \times 10^{14}$ W/cm^2, $\omega = 0.057$ a.u., $\lambda = 800$ nm, $T = 2.7$ fs, six optical cycles.

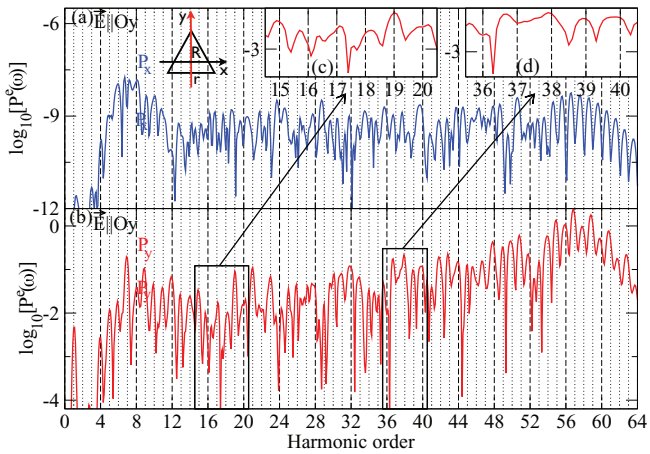

FIG. 8. (Color online) (a), (b) Molecular high-order-harmonic (MHOHG) spectra of H_3^{2+} with fixed nuclei at $r = R = 5$ a.u. [blue, $P_x^e(\omega)$ and red, $P_y^e(\omega)$], with (c),(d) zoom of the harmonics in the plateau region for $P_y^e(\omega)$. Laser-pulse conditions: $\vec{E}||Oy$, $I = 3 \times 10^{14}$ W/cm^2, $\omega = 0.057$ a.u., $\lambda = 800$ nm, $T = 2.7$ fs, six optical cycles.

the components $P_x^e(\omega)$ and $P_y^e(\omega)$ given by

$$\eta = \arccos\left[\frac{\mathbb{R}(P_{xy})}{|P_{xy}|}\right], \tag{14}$$

with $P_{xy} = P_x^e(\omega)/P_y^e(\omega)$, as illustrated in Fig. 5(d). Very interestingly, the relative phase becomes stable (with respect to the frequency, i.e., phase locking) and with a nonzero value at high-order harmonics (in our case, $\eta \approx \pi/2$). These are the two conditions to generate elliptically polarized attosecond pulses by superposition of these harmonics. The calculated ellipticity for these harmonics is $\varepsilon \approx 0.1$ [green circles in Fig. 5(d)]; a higher value of ε would require the same intensity for $P_x^e(\omega)$ and $P_y^e(\omega)$. Thus, elliptically polarized harmonics (in the cutoff region) are generated when a linear pulse is applied along the basis nuclear axis (parallel to r coordinate) of a triangular molecule. Elliptically polarized high-order harmonics near the cutoff have also been generated with a linear drive laser field in molecular ring-current states [38]. For $\vec{E}||Oy$, the situation is very different and the $P_y^e(\omega)$, parallel to the laser-pulse polarization, is 20 orders higher (10 orders for the static case) than the $P_x^e(\omega)$ perpendicular component. In fact, the intensity of the perpendicular component $P_x^e(\omega)$ should be strictly zero since the laser-pulse polarization is along a symmetry axis of both the D_{3h} and C_{2v} configurations of the triangular molecule. The calculated value of magnitude $\approx 10^{-25}$ is negligible, an artifact of the numerical simulations. We conclude that harmonics are linearly polarized when $\vec{E}||Oy$ is applied. Similar trends in $P_x^e(\omega)$ and $P_y^e(\omega)$ were also observed for a two-electron system, H_3^+, in a static, stretched configuration [24].

Another important observation is the order of the harmonics. In Fig. 6, with $\vec{E}||Oy$, the harmonics [$P_y^e(\omega)$] in the cutoff region are exclusively *even*. When looking at lower order harmonics [Figs. 6(c) and 6(d)], one can see a redshift in the harmonics. This redshift increases with harmonic order in the plateau region. In fact, odd harmonics exist too, but at weaker intensity, and vanish at higher order into the shifted

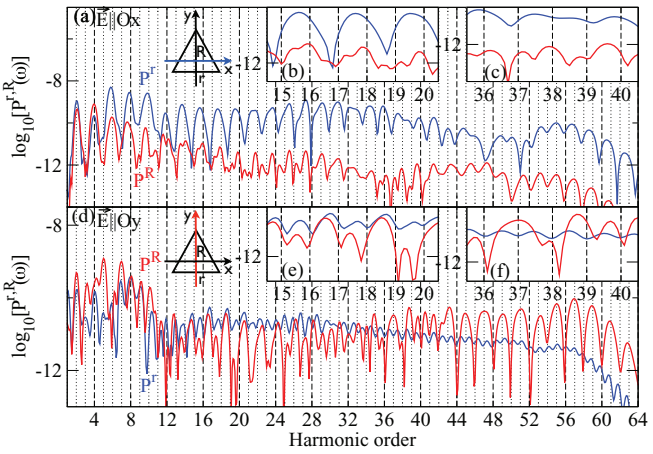

FIG. 9. (Color online) Fourier transform of the nuclear accelerations along the R (red solid line) and the r (blue solid line) coordinates for $\vec{E}||Ox$ (upper panels) and $\vec{E}||Oy$ (lower panels). Insets (b), (c), (e), and (f) show the harmonics in the plateau region. Laser-pulse conditions: $I = 3 \times 10^{14}$ W/cm^2, $\omega = 0.057$ a.u., $\lambda = 800$ nm, $T = 2.7$ fs, six optical cycles.

even harmonics. This redshift is induced by the fact that the ionization, and therefore the harmonics emission, occur only once the molecule has moved to large internuclear distances, which happens at the end of the laser pulse (i.e., in the falling ramp of the pulse envelope) [39]. As for $\vec{E}||Ox$, shown in Fig. 5, the harmonics $[P^e_x(\omega)]$ in the cutoff region are *odd*. The harmonics are also odd at very low order and are then redshifted in the plateau region [Figs. 5(b) and 5(c)]. We note that the non-negligible perpendicular harmonics $P^e_y(\omega)$ are shifted as well, but this shift is different from the one on $P^e_x(\omega)$ because of the asymmetry in the Coulomb potential in the x and y directions. For the static case ($\vec{E}||Ox$ [Fig. 7] and $\vec{E}||Oy$ [Fig. 8]), odd and even harmonics are observed at all orders. The redshift, although existing in the plateau region (see inset panels of Figs. 7 and 8), is much less visible. In fact, in this stretched static configuration, harmonics are emitted during the total pulse, including the rising ramp and high-amplitude portion of the pulse envelope, where a redshift is not visible [39].

The Fourier transform of the nuclear accelerations [a^r,a^R; Eq. (13a)] are also calculated and shown in Fig. 9. While looking more in detail, one can observe odd harmonics in $P^R(\omega)$ (N_1 motion to C_{2v}) for both laser polarizations, while in $P^r(\omega)$ (N_2–N_3 motion), odd harmonics are observed for $\vec{E}||Ox$ and weak odd and even harmonics are observed for $\vec{E}||Oy$. The intensity is stronger in $P^r(\omega)$ with the $\vec{E}||Ox$, and in $P^R(\omega)$ with the $\vec{E}||Oy$ (i.e., favored intensity for the nuclear coordinate parallel to the laser-pulse polarization). We observe that for $\vec{E}||Oy$, the perpendicular component $P^r(\omega)$ does not become negligible, as is the case for the electron part $P^e_x(\omega)$, because the nuclei are always moving in both the r and R directions due to strong nuclear repulsion, so there should be a contribution from both coordinates. Note that for $P^r(\omega)$ with $\vec{E}||Ox$, a similar redshift is observed where low even harmonics are slowly shifted to odd order in the plateau region. For $P^R(\omega)$ with $\vec{E}||Oy$, odd and even harmonics are observed at low order, where even harmonics weaken in the plateau region and vanish into the shifted odd harmonics. The nuclear acceleration reflects the effect of electron recollisions directly on the nuclear dynamics, as seen in H_2 [35]. In sum, electron and nuclei behave in a correlated way where, with $\vec{E}||Ox$, both parallel and perpendicular components participate in the dynamics, while with $\vec{E}||Oy$, essentially only the parallel component is involved.

A time-frequency analysis, via Gabor transforms [Eq. (12)], of the electron acceleration gives an estimated electron recollision time. The same Gabor transformation can be applied to the nuclear accelerations and provides complementary information of the nuclear motion during the electron recollision event. The time-frequency profiles are shown in Figs. 10 and 11 for the harmonics in the plateau region ($N = 25$, left panels) and in the cutoff region ($N = 58$, right panels) for $\vec{E}||Ox$ and $\vec{E}||Oy$, respectively. It is important to note that for $\vec{E}||Ox$, where comparable intensity of $P^e_x(\omega)$ and $P^e_y(\omega)$ [although $P^e_x(\omega) > P^e_y(\omega)$] in the MHOHG spectrum was observed, the Gabor transform of the electron acceleration gives a non-negligible value of the perpendicular component (a^e_y), with exactly the same peak position, although it is much weaker in intensity. This observation holds for the static and the dynamic cases. As for $\vec{E}||Oy$, where $P^e_x(\omega)$ was negligible (or much weaker) in the MHOHG spectrum, the Gabor transform of the perpendicular component, a^e_x, is also negligible for the static and the dynamic cases. For both polarizations, in the

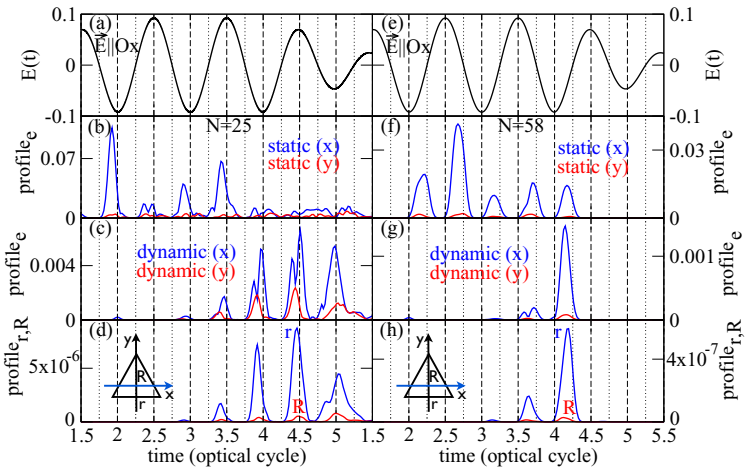

FIG. 10. (Color online) Left panels: Gabor analysis for harmonics in the plateau region ($N = 25$). Right panels: Gabor analysis for harmonics in the cutoff region ($N = 58$). (a), (e) Electric laser pulse $\vec{E}||Ox$ as a function of time. Gabor transform of the electron acceleration with (b)–(f) fixed nuclei ($r = R = 5$ a.u.) and (c), (g) moving nuclei. (d), (h) Gabor transform of the nuclear accelerations in the R and r coordinates. For all panels: blue solid line for $x(r)$ component and red solid line for $y(R)$ component. Laser-pulse conditions: $\vec{E}||Ox$, $I = 3 \times 10^{14}$ W/cm^2, $\omega = 0.057$ a.u., $\lambda = 800$ nm, $T = 2.7$ fs, six optical cycles.

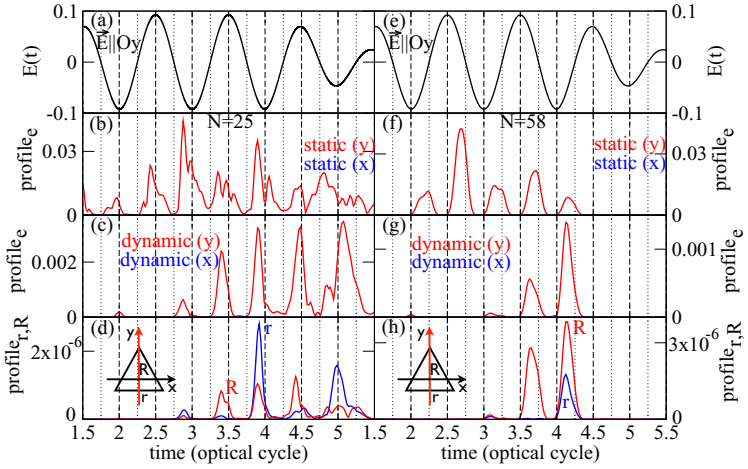

FIG. 11. (Color online) Left panels: Gabor analysis for harmonics in the plateau region ($N = 25$). Right panels: Gabor analysis for harmonics in the cutoff region ($N = 58$). (a),(e) Electric laser pulse $\vec{E}||Oy$ as a function of time. Gabor transform of the electron acceleration with (b)–(f) fixed nuclei ($r = R = 5$ a.u.) and (c),(g) moving nuclei. (d),(h) Gabor transform of the nuclear accelerations in the R and r coordinates. For all panels: blue solid line for $x(r)$ component and red solid line for $y(R)$ component. Laser-pulse conditions: $\vec{E}||Oy$, $I = 3 \times 10^{14}$ W/cm^2, $\omega = 0.057$ a.u., $\lambda = 800$ nm, $T = 2.7$ fs, six optical cycles.

static case [Figs. 10(b) and 10(f), and Figs. 11(b) and 11(f)], recollision events occur at $t_{\rm rec} = 0.7T$ after an extremum and before zeros of the electric field in the cutoff region, and at the extrema of the electric field in the plateau region, in agreement with the semiclassical recollision model [3,5]. In the dynamic case [Figs. 10(c) and 10(g), and Figs. 11(c) and 11(g)], the ionization occurs only after three optical cycles. Consequently, four main peaks are observed in the plateau region (left panels of Figs. 10 and 11). In the cutoff region (right panels of Figs. 10 and 11), two main peaks are observed at $t^c_{\rm rec_1} = 3.7T$ and $t^c_{\rm rec_2} = 4.2T$, indicating two main recollision events. This is in correlation with ionization events that are important at $3T$ and $3.5T$ [see Fig. 2(a)] when the nuclei have moved to large distances [see Figs. 2(c) and 2(d)]. In fact, nuclear and electron motion are clearly correlated: time-frequency profiles show important similarities. Still, in the cutoff region, one observes that in the nuclear acceleration profiles [Figs. 10(h) and 11(h)], for the dynamic case, two main peaks appear in the R coordinates (N_1 motion) at the same times $t^c_{\rm rec_1}$ and $t^c_{\rm rec_2}$ for both polarizations, while there are two peaks in the r coordinate (N_2–N_3 motion) only with $\vec{E}||Ox$. The peak at $t^c_{\rm rec_1}$ is absent with $\vec{E}||Oy$ in the r coordinate, perpendicular to the y axis. When referring to Fig. 4, with $\vec{E}||Oy$, one can see from the calculated electron-density snapshots that at $t^c_{\rm rec_1}$, the electron density is localized on the upper N_1 proton. Therefore, only the R coordinate, perpendicular to N_2–N_3 motion, contributes in this recollision event and the harmonics come mainly by recombination with the N_1 H atom. At $t^c_{\rm rec_2}$, the electronic density is delocalized over the three protons and both r and R (N_1, N_2, N_3 H atoms) coordinates contribute to the recollision event. This can also be understood by the oscillation of periodicity ω observed in the proton acceleration $a^r_y(t)$ [Fig. 2(h)], where for every cycle ($m = 1$), the chemical bond along the r coordinate is strengthened. In the case of $\vec{E}||Ox$ (see Fig. 3), the electron density is delocalized over the three protons at $t^c_{\rm rec_1}$ and $t^c_{\rm rec_2}$, and therefore the two nuclear coordinates, r and R, contribute to the recollision event. Similar dynamics occurs in the plateau region [Figs. 10(d) and 11(d)], where, in this case, four main peaks in the R coordinate at the same recollision times are observed in the electron acceleration profile for both polarizations. In the r coordinate, two of those main peaks weaken with $\vec{E}||Oy$, and this can be explained again by a localization of the electron on the upper N_1 proton at those specific times ($m = 1/2$ in Fig. 4). Returning to $\vec{E}||Ox$, from the two recollision events observed in the cutoff region, the second one at $t^c_{\rm rec_2}$ is clearly more intense. We recall that with this specific polarization, the harmonics generated in the cutoff region are found to be elliptically polarized (Fig. 5). Therefore, from the time-frequency analysis, we can see that a nearly isolated attosecond pulse, elliptically polarized, can be generated with a linearly polarized laser pulse aligned parallel to a bond of the triangular molecular ion.

IV. CONCLUSION

We have presented the full 2D non-Born-Oppenheimer electron-nuclear dynamics of the triatomic molecular ion H_3^{2+}, an important intermediate to the Coulomb explosion of $H_3{}^+$, in an intense few-cycle laser pulse at 800 nm wavelength. The simulations have been performed for two electric-field polarizations, x polarization parallel to one H–H bond and y polarization perpendicular to that bond and along the third proton direction. Our first result is that at the intensities $I \geqslant 3 \times 10^{14}$ W/cm^2, rapid ionization occurs after three cycles, when proton internuclear distances reach each r and $R \approx 4$ a.u., where there is a three-photon resonance with the degenerate electronic E state in D_{3h} symmetry, in agreement with experimental results [17,20]. After five cycles, the molecular ion has expanded by dissociative ionization by $\Delta r \approx 4$ a.u. (0.2 nm) and $\Delta R \approx 3$ a.u. (0.16 nm), corresponding to velocities 0.14 Å/fs and 0.12 Å/fs. Calculations of the nonperturbative laser-induced accelerations for the time-dependent electron $a^e_{x(y)}(t)$ show that these follow the pulse field in phase, thus implying the dominance of the Coulomb fields. The proton acceleration $a^R(t)$ is in phase with the field, $\vec{E}||Ox$ and $\vec{E}||Oy$, but oscillates with twice the field frequency, with minima at zeros of the field corresponding to vanishing perturbation. However, $a^r(t)$, along the H–H (N_2–N_3) bond, is out of phase with the field $\vec{E}||Oy$ perpendicular to that bond, and correlates with electron transfer from the outer (N_1) proton to the H–H (N_2–N_3) bond, thus reinforcing this bond. The observed oscillations at the field frequency are indicative of the creation and destruction of the chemical bond on the near-fs time scale.

The coupled electron-nuclear dynamics has a strong influence on the MHOHG spectra. The following important observations can be made from these nonperturbative simulations: First, harmonics are mainly *even* for $\vec{E}||Oy$ and *odd* for $\vec{E}||Ox$, while they are even and odd in the static Born-Oppenheimer configuration for a stretched molecule at $r = R = 5$ a.u. Second, there is a redshift in the harmonics, due to the fact that the electron ionization dynamics starts in the stretched configuration of the molecular ion which is reached only in the second half of the pulse envelope where pulse intensities decrease. Third, in general, for $\vec{E}||Ox$ (parallel to a bond of the triangular molecule), perpendicular harmonics $[P_y^e(\omega)]$ are generated and, in particular, the harmonics near the cutoff are elliptically polarized.

The time-frequency analysis of all accelerations, electron $a^e(\omega)$ and protons $a^R(\omega)$, $a^r(\omega)$, shows that low harmonics ($N < 30$) are created by four recollisions at times 3.5,4,4.5, and 5 cycles, i.e., at extrema of the laser field. High-order harmonics near the cutoff ($N > 30$) are created by a nearly single recollision at a 4.25 cycle where the field is zero. These results confirm the different recollisions at low and high energies in concert with the response of the nuclear motion along r (H–H) bond and R (movement of perpendicular N_1 proton), which coincide with the time of electronic harmonic emission.

ACKNOWLEDGMENTS

We thank Dr. K. J. Yuan and Dr. X. B. Bian for valuable discussions. We also acknowledge RQCHP, SciNet, and Compute Canada for access to massively parallel computer clusters, and the Natural Sciences and Engineering Research Council of Canada (NSERC) and Canadian Institute for Photonic Innovations (CIPI) for financial support of this research in its ultrafast science program. CL acknowledges also the Fonds Québécois de la Recherche sur la Nature et les Technologies (FQRNT) for financial support.

APPENDIX A

We consider the molecular system H_3^{2+}, composed of four particles (three nuclei forming a triangle in a C_{2v} symmetry and one electron) of coordinate $\vec{r}_{N_1},\vec{r}_{N_2},\vec{r}_{N_3},\vec{r}_e$ and mass $m_{N_1} = m_{N_2} = m_{N_3}$ and m_e, respectively. We define four new coordinates: the center-of-mass coordinate of the four particles, $\vec{R}_{cm}$, the relative coordinate of the electron with respect to the center of mass of the three nuclei, $\vec{R}_{el}$, the relative coordinate of the nucleus at the top of the triangle with respect to the center of mass of the two nuclei forming the basis of the triangle, $\vec{R}_H$, and the relative coordinate of the two nuclei forming the basis of the triangle, $\vec{R}_B$. The total mass of the system is $M_T = m_e + m_{N_1} + m_{N_2} + m_{N_3}$, the mass of the nuclei is $M_N = m_{N_1} + m_{N_2} + m_{N_3}$, and the mass of the nuclei forming the basis of the triangle is $M_B = m_{N_2} + m_{N_3}$. Atomic units are used, i.e., $\hbar = m_e = 1$.

We thus have a system of four equations with four unknowns:

$$M_T\vec{R}_{cm} = m_e\vec{r}_e + m_{N_1}\vec{r}_{N_1} + m_{N_2}\vec{r}_{N_2} + m_{N_3}\vec{r}_{N_3}, \tag{A1a}$$

$$M_N\vec{R}_{el} = M_N\vec{r}_e - m_{N_1}\vec{r}_{N_1} - m_{N_2}\vec{r}_{N_2} - m_{N_3}\vec{r}_{N_3}, \tag{A1b}$$

$$M_B\vec{R}_H = M_B\vec{r}_{N_1} - m_{N_2}\vec{r}_{N_2} - m_{N_3}\vec{r}_{N_3}, \tag{A1c}$$

$$\vec{R}_B = \vec{r}_{N_2} - \vec{r}_{N_3}, \tag{A1d}$$

from which we obtain

$$\vec{r}_e = \vec{R}_{cm} + \frac{M_N}{M_T}\vec{R}_{el}, \tag{A2a}$$

$$\vec{r}_{N_1} = R_{cm} - \frac{m_e}{M_T}\vec{R}_{el} + \frac{M_B}{M_N}\vec{R}_H, \tag{A2b}$$

$$\vec{r}_{N_2} = R_{cm} - \frac{m_e}{M_T}\vec{R}_{el} - \frac{m_{N_1}}{M_N}\vec{R}_H + \frac{m_{N_3}}{M_B}\vec{R}_B, \tag{A2c}$$

$$\vec{r}_{N_3} = \vec{R}_{cm} - \frac{m_e}{M_T}\vec{R}_{el} - \frac{m_{N_1}}{M_N}\vec{R}_H - \frac{m_{N_2}}{M_B}\vec{R}_B. \tag{A2d}$$

The Hamiltonian (see Appendix B for details) is

$$\hat{H} = \hat{T} + V. \tag{A3}$$

The kinetic-energy operator $\hat{T} = \hat{T}_N + \hat{T}_{el}$ is composed of the nuclear part

$$\hat{T}_N = -\frac{1}{2\mu_{R_H}}\frac{\partial^2}{\partial R_H^2} - \frac{1}{2\mu_{R_B}}\frac{\partial^2}{\partial R_B^2}, \tag{A4}$$

and the electronic part

$$\hat{T}_{el} = -\frac{1}{2\mu_{R_{el}}}\frac{\partial^2}{\partial R_{el}^2}, \tag{A5}$$

with $\mu_{R_H} = \frac{m_{N_1}M_B}{M_N}$, $\mu_{R_B} = \frac{m_{N_2}m_{N_3}}{M_B}$, and $\mu_{el} = \frac{m_eM_N}{M_T}$. The potential $V = V_{eN} + V_{NN} + V_{\rm int}$ is composed of the electron-nuclei attraction potential,

$$V_{eN}(\vec{r}_e,\vec{r}_{N_1},\vec{r}_{N_2},\vec{r}_{N_3}) = -[(\vec{r}_e - \vec{r}_{N_1})^2 + c_{eN}]^{-1/2} + [(\vec{r}_e - \vec{r}_{N_2})^2 + c_{eN}]^{-1/2} + [(\vec{r}_e - \vec{r}_{N_3})^2 + c_{eN}]^{-1/2},$$

$$V_{eN}(\vec{R}_{el},\vec{R}_H,\vec{R}_B) = -\left[\left(\vec{R}_{el} - \frac{M_B}{M_N}\vec{R}_H\right)^2 + c_{eN}\right]^{-1/2} - \left[\left(\vec{R}_{el} + \frac{m_{N_1}}{M_N}\vec{R}_H - \frac{m_{N_3}}{M_B}\vec{R}_B\right)^2 + c_{eN}\right]^{-1/2}$$

$$- \left[\left(\vec{R}_{el} + \frac{m_{N_1}}{M_N}\vec{R}_H + \frac{m_{N_2}}{M_B}\vec{R}_B\right)^2 + c_{eN}\right]^{-1/2}, \tag{A6}$$

the nuclear repulsion potential,

$$V_{NN}(\vec{r}_{N_1},\vec{r}_{N_2},\vec{r}_{N_3}) = [(\vec{r}_{N_1} - \vec{r}_{N_2})^2 + c_{NN}]^{-1/2} + [(\vec{r}_{N_2} - \vec{r}_{N_3})^2 + c_{NN}]^{-1/2} + [(\vec{r}_{N_3} - \vec{r}_{N_1})^2 + c_{NN}]^{-1/2},$$

$$V_{NN}(\vec{R}_H,\vec{R}_B) = \left[\left(\vec{R}_H - \frac{M_{N_3}}{M_B}\vec{R}_B\right)^2 + c_{NN}\right]^{-1/2} + \left(\vec{R}_B^2 + c_{NN}\right)^{-1/2} + \left[\left(-\vec{R}_H - \frac{m_{N_2}}{M_B}\vec{R}_B\right)^2 + c_{NN}\right]^{-1/2}, \tag{A7}$$

with c_{eN} and c_{NN} as soft-core parameters, and the interaction potential

$$V_{\rm int}(\vec{r}_e,\vec{r}_{N_1},\vec{r}_{N_2},\vec{r}_{N_3}) = -\vec{D}\cdot\vec{E}(t) = -\left(\sum_i q_i\vec{r}_i\right)\cdot\vec{E}(t) = -(-\vec{r}_e+\vec{r}_{N_1}+\vec{r}_{N_2}+\vec{r}_{N_3})\cdot\vec{E}(t),$$

$$\begin{aligned} V_{\rm int}(\vec{R}_{el}) &= -\Big(-\vec{R}_{cm}-\frac{M_N}{M_T}\vec{R}_{el}+\vec{R}_{cm}-\frac{m_e}{M_T}\vec{R}_{el}+\frac{M_B}{M_N}\vec{R}_H+\vec{R}_{cm}-\frac{m_e}{M_T}\vec{R}_{el}-\frac{m_{N_1}}{M_N}\vec{R}_H \\ &\quad +\frac{m_{N_3}}{M_B}\vec{R}_B+\vec{R}_{cm}-\frac{m_e}{M_T}\vec{R}_{el}-\frac{m_{N_1}}{M_N}\vec{R}_H-\frac{m_{N_2}}{M_B}\vec{R}_B\Big)\cdot\vec{E}(t) \\ &= -\left(2\vec{R}_{CM}-\frac{3m_e+M_N}{M_T}\vec{R}_{el}+\frac{M_B-m_{N_1}-m_{N_1}}{M_N}\vec{R}_H+\frac{m_{N_3}-m_{N_2}}{m_B}\vec{R}_B\right)\cdot\vec{E}(t)=\lambda_{el}\vec{R}_{el}\cdot\vec{E}(t), \end{aligned} \quad \text{(A8)}$$

where $\vec{D}$ is the dipole, with q_i and $\vec{r}_i$ the charge and the position of the i^e particle, and $\vec{E}(t)$ the electric field. The charge of the nucleus is $+1$ and the charge of the electron is -1. The factor of mass is $\lambda_{el}=\frac{2m_e+M_T}{M_T}$. The acceleration of the dipole is

$$\frac{d^2}{dt^2}\vec{D} = \frac{1}{i}\left[\frac{d}{dt}\vec{D},H\right] = \frac{1}{i}[-\phi_{el}\vec{p}_{el},H] = \phi_{el}\frac{\partial H}{\partial\vec{R}_{el}}. \quad \text{(A9)}$$

Note that in the paper, we use the following conventions: $m_e=1, |\vec{R}_H|=R, |\vec{R}_B|=r$, and $\vec{R}_{\rm rel}=x\vec{e}_x+y\vec{e}_y$, where $\vec{e}_x$ and $\vec{e}_y$ are unit vectors.

APPENDIX B

From the classical Lagrangian, we can write

$$\begin{aligned} L &= -\tfrac{1}{2}\big(m_e\dot{\vec{r}}_e^2+m_{N_1}\dot{\vec{r}}_{N_1}^2+m_{N_2}\dot{\vec{r}}_{N_2}^2+m_{N_3}\dot{\vec{r}}_{N_3}^2\big) \\ &\quad -V(\vec{r}_e,\vec{r}_{N_1},\vec{r}_{N_2},\vec{r}_{N_3}). \end{aligned} \quad \text{(B1)}$$

By replacing Eqs. (A2a)–(A2d) in Eq. (B1), we obtain

$$\begin{aligned} L &= -\tfrac{1}{2}\big(M_T\dot{\vec{R}}_{cm}^2+\mu_{el}\dot{\vec{R}}_{el}^2+\mu_{R_H}\dot{\vec{R}}_H^2+\mu_{R_B}\dot{\vec{R}}_B^2\big) \\ &\quad -V(\vec{R}_{el},\vec{R}_H,\vec{R}_B), \end{aligned} \quad \text{(B2)}$$

with mass factors $\mu_{el}=\frac{m_eM_N}{M_T}$, $\mu_{R_H}=\frac{m_{N_1}M_B}{M_N}$, and $\mu_{R_B}=\frac{m_{N_3}m_{N_2}}{M_B}$. The momentum (classical) is $\vec{p}_k=\frac{\partial L}{\partial\dot{\vec{R}}_k}$, such that the total momentum is

$$\begin{aligned} \vec{p}_{\rm tot} &= -(M_T\dot{\vec{R}}_{cm}+\mu_{el}\dot{\vec{R}}_{el}+\mu_{R_H}\dot{\vec{R}}_H+\mu_{R_B}\dot{\vec{R}}_B) \\ &= \vec{p}_{cm}+\vec{p}_{el}+\vec{p}_H+\vec{p}_B, \end{aligned} \quad \text{(B3)}$$

and the total Hamiltonian (classical) is

$$\begin{aligned} H_{\rm tot} &= \frac{\vec{p}_{cm}^2}{2M_T}+\frac{\vec{p}_{el}^2}{2\mu_{el}}+\frac{\vec{p}_{R_H}^2}{2\mu_{R_H}}+\frac{\vec{p}_{R_B}^2}{2\mu_{R_B}}+V(\vec{R}_{el},\vec{R}_H,\vec{R}_B) \\ &= H_{cm}+H_{\rm rel}. \end{aligned} \quad \text{(B4)}$$

In the center-of-mass referential, $\vec{p}_{cm}=0, H_{cm}=0$, such that

$$H_{\rm tot} = \frac{\vec{p}_{el}^2}{2\mu_{el}}+\frac{\vec{p}_{R_H}^2}{2\mu_{R_H}}+\frac{\vec{p}_{R_B}^2}{2\mu_{R_B}}+V(\vec{R}_{el},\vec{R}_H,\vec{R}_B). \quad \text{(B5)}$$

In quantum mechanics, the position and the momentum are operators ($[\hat{r},\hat{p}]=i\hbar$) and the total Hamiltonian is

$$\begin{aligned} \hat{H}_{\rm tot} &= \frac{\hat{p}_{cm}^2}{2M_T}+\frac{\hat{p}_{el}^2}{2\mu_{el}}+\frac{\hat{p}_{R_H}^2}{2\mu_{R_H}}+\frac{\hat{p}_{R_B}^2}{2\mu_{R_B}}+V(\hat{R}_{el},\hat{R}_H,\hat{R}_B) \\ &= \hat{H}_{cm}+\hat{H}_{\rm rel}. \end{aligned} \quad \text{(B6)}$$

We can separate the center-of-mass motion, $[\hat{H}_{cm},\hat{H}_{\rm rel}]=0, [\hat{H}_{\rm rel},\hat{H}_{\rm tot}]=0, [\hat{H}_{\rm tot},\hat{H}_{cm}]=0$, and the relative motion between the four particles is given by $\hat{H}_{\rm rel}$,

$$\hat{H}=\hat{H}_{\rm rel} = \frac{\hat{p}_{el}^2}{2\mu_{el}}+\frac{\hat{p}_{R_H}^2}{2\mu_{R_H}}+\frac{\hat{p}_{R_B}^2}{2\mu_{R_B}}+V(\hat{R}_{el},\hat{R}_H,\hat{R}_B). \quad \text{(B7)}$$

[1] A. D. Bandrauk and M. Ivanov, *Quantum Dynamic Imaging* (Springer, New York, 2011).
[2] F. Kelkensberg *et al.*, Phys. Rev. Lett. **103**, 123005 (2009).
[3] P. B. Corkum, Phys. Rev. Lett. **71**, 1994 (1993).
[4] A. D. Bandrauk, S. Barmaki, and G. L. Kamta, Phys. Rev. Lett. **98**, 013001 (2007).
[5] F. Krausz and M. Ivanov, Rev. Mod. Phys. **81**, 163 (2009).
[6] A. D. Bandrauk and J. Ruel, Phys. Rev. A **59**, 2153 (1999).
[7] A. D. Bandrauk and F. Légaré, *Progress in Ultrafast Intense Laser Science VIII* (Springer, Tokyo, 2012), Chap. 2.
[8] X.-B. Bian, L.-Y. Peng, and T.-Y. Shi, Phys. Rev. A **78**, 053408 (2008).
[9] I. Kawata, H. Kono, and A. D. Bandrauk, Phys. Rev. A **64**, 043411 (2001).
[10] A. D. Bandrauk, S. Chelkowski, and I. Kawata, Phys. Rev. A **67**, 013407 (2003).
[11] D. Strasser, L. Lammich, S. Krohn, M. Lange, H. Kreckel, J. Levin, D. Schwalm, Z. Vager, R. Wester, A. Wolf, and D. Zajfman, Phys. Rev. Lett. **86**, 779 (2001).
[12] A. E. Orel and K. C. Kulander, Phys. Rev. Lett. **71**, 4315 (1993).
[13] T. R. Geballe and T. Oka, Nature (London) **384**, 334 (1996).
[14] E. Lötstedt and K. Midorikawa, Phys. Rev. A **88**, 041402(R) (2013).
[15] P. M. Kraus, M. C. Schwarzer, N. Schirmel, G. Urbasch, G. Frenking, and K.-M. Weitel, J. Chem. Phys. **134**, 114302 (2011).
[16] H. Xu, C. Marceau, K. Nakai, T. Okino, S.-L. Chin, and K.Yamanouchi, J. Chem. Phys. **133**, 071103 (2010).

[17] J. McKenna, A. M. Sayler, B. Gaire, N. G. Johnson, K. D. Carnes, B. D. Esry, and I. Ben-Itzhak, Phys. Rev. Lett. **103**, 103004 (2009).
[18] A. M. Sayler, J. McKenna, B. Gaire, N. G. Kling, K. D. Carnes, and I. Ben-Itzhak, Phys. Rev. A **86**, 033425 (2012).
[19] J. D. Alexander, C. R. Calvert, R. King, O. Kelly, L. Graham, W. A. Bryan, G. R. A. J. Nemeth, W. R. Newell, C. A. Froud, I. C. E. Turcu, E. Spingate, I. D. Williams, and J. B. Greenwood, J. Phys. B **42**, 141004 (2009).
[20] B. Gaire, J. McKenna, M. Zohrabi, K. D. Carnes, B. D. Esry, and I. Ben-Itzhak, Phys. Rev. A **85**, 023419 (2012).
[21] E. Lötstedt, T. Kato, and K. Yamanouchi, Phys. Rev. Lett. **106**, 203001 (2011); Phys. Rev. A **85**, 053410 (2012).
[22] S. Wuster, A. Eisfeld, and J. M. Rost, Phys. Rev. Lett. **106**, 153002 (2011).
[23] H. DeRaedt, K. Michielsen, and K. Hess, Phys. Rev. A **85**, 012101 (2012).
[24] D. S. Tchitchekova, H. Lu, S. Chelkowski, and A. D. Bandrauk, J. Phys. B **44**, 065601 (2011).
[25] L. S. Cederbaum and M. Basler, Phys. Rev. Lett. **103**, 133001 (2009).
[26] F. He, C. Ruiz, and A. Becker, Phys. Rev. A **75**, 053407 (2007).
[27] R. Kosloff and H. Tal-Ezer, Chem. Phys. Lett. **127**, 223 (1986).
[28] L. P. Viegas, A. Alijah, and A. J. Varandas, J. Chem. Phys. **126**, 074309 (2007).
[29] P. Barragán, L. F. Errea, A. Macía, L. Méndez, I. Rabadán, and A. Riera, J. Chem. Phys. **124**, 184303 (2006).
[30] A. Ichihara and K. Yokoyama, J. Chem. Phys. **103**, 2109 (1995).
[31] S. Chelkowski, C. Foisy, and A. D. Bandrauk, Phys. Rev. A **57**, 1176 (1998).
[32] A. D. Bandrauk, S. Chelkowski, D. J. Diestler, J. Manz, and K.-J. Yuan, Phys. Rev. A **79**, 023403 (2009).
[33] C. Chandre, S. Wiggins, and T. Uzer, Physica D **181**, 171 (2003).
[34] P. Antoine, B. Piraux, and A. Maquet, Phys. Rev. A **51**, R1750 (1995).
[35] A. D. Bandrauk, S. Chelkowski, and H. Lu, Chem. Phys. **414**, 73 (2013).
[36] A. J. Verhoef, A. V. Mitrofanov, E. E. Serebryannikov, D. V. Kartashov, A. M. Zheltikov, and A. Baltuska, Phys. Rev. Lett. **104**, 163904 (2010).
[37] X.-B. Bian and A. D. Bandrauk, Phys. Rev. Lett. **105**, 093903 (2010).
[38] X. Xie, A. Scrinzi, M. Wickenhauser, A. Baltuska, I. Barth, and M. Kitzler, Phys. Rev. Lett. **101**, 033901 (2008).
[39] X.-B. Bian and A. D. Bandrauk, Phys. Rev. A **83**, 041403(R) (2011).